Tide model accuracy in the Amundsen Sea, Antarctica, from radar interferometry observations of ice shelf motion

Tide model accuracy in the Amundsen Sea, Antarctica, from radar interferometry observations of ice shelf motion

M. McMillan,[1,2] A. Shepherd,[1] P. Nienow,[2] and A. Leeson[1]

Received 13 May 2011; revised 10 August 2011; accepted 15 August 2011; published 5 November 2011.

[1] This study assesses the accuracy of tide model predictions in the Amundsen Sea sector of West Antarctica. Tide model accuracy in this region is poorly constrained, yet tide models contribute to simulations of ocean heat transfer and to the removal of tidal signals from satellite observations of ice shelves. We use two satellite-based interferometric synthetic aperture radar (InSAR) methods to measure the tidal motion of the Dotson Ice Shelf at multiple epochs: a single-difference technique that measures tidal displacement and a double-difference technique that measures changes in tidal displacement. We use these observations to evaluate predictions from three tide models (TPXO7.1, CATS2008a_opt, and FES2004). All three models perform comparably well, exhibiting root-mean-square deviations from the observations of ~9 cm (single-difference technique) and ~10 cm (double-difference technique). Care should be taken in generalizing these error statistics because (1) the Dotson Ice Shelf experiences relatively small semidiurnal tides and (2) our observations are not sensitive to all tidal constituents. An error analysis of our InSAR-based methods indicates measurement errors of 7 and 4 cm for the single- and double-difference techniques, respectively. A model-based correction for the effect of fluctuations in atmospheric pressure yields an ~6% improvement in the agreement between tide model predictions and observations. This study suggests that tide model accuracy in the Amundsen Sea is comparable to other Antarctic regions where tide models are better constrained. These methods can be used to evaluate tide models in other remote Antarctic waters.

Citation: McMillan, M., A. Shepherd, P. Nienow, and A. Leeson (2011), Tide model accuracy in the Amundsen Sea, Antarctica, from radar interferometry observations of ice shelf motion, *J. Geophys. Res.*, *116*, C11008, doi:10.1029/2011JC007294.

1. Introduction

[2] Floating ice shelves fringe around one third of Antarctica's coastline [*Sugden*, 2009] and regulate the rate at which ice mass is lost from the continent. As a consequence of being in contact with both the ocean and the warmer air around the ice sheet's margin, they are particularly sensitive to changes in atmospheric [*Vaughan and Doake*, 1996] and oceanic [*Rignot and Jacobs*, 2002; *Shepherd et al.*, 2004] conditions. Many studies have documented late twentieth century ice shelf retreat [*Vaughan and Doake*, 1996; *Rignot*, 1998; *Cook and Vaughan*, 2010] and collapse [*Rott et al.*, 1996; *Scambos et al.*, 2009], and have identified the ocean and atmosphere as having driven these changes. Although the steric effect of ice shelf mass loss upon sea level is small [*Shepherd et al.*, 2010], an indirect dynamical response [*De Angelis and Skvarca*, 2003; *Rignot et al.*, 2004, 2005] resulting from reduced buttressing of upstream ice may provide a much larger sea level contribution [*Payne et al.*, 2004; *Pfeffer et al.*, 2008]. Until this mechanism is incorporated into model predictions of the response of the Antarctic Ice Sheet (AIS) to changing climatic conditions, the future sea level contribution of the AIS remains uncertain. In this context, continued monitoring of ice shelf behavior is essential.

[3] Tide models contribute to our understanding of the response of the AIS to changes in its surrounding ocean environment. Tides are one of the principle drivers of ocean mixing beneath ice shelves and therefore tide models are an essential component of modeling studies of ice-ocean interactions [*Makinson et al.*, 2011]. Tide models are also used to correct for the tidal signal in many satellite-based interferometric synthetic aperture radar (InSAR) methods to estimate ice shelf flow [*Rignot and Jacobs*, 2002; *Joughin et al.*, 2003; *Rignot et al.*, 2004; *Vieli et al.*, 2006]. Such methods are used to assess ice shelf stability and the processes through which ice shelves interact with the atmosphere, the ocean and grounded ice upstream [*Joughin and Padman*, 2003; *Vieli et al.*, 2007]. In a similar fashion, tide models have been used to remove unwanted tidal signals from altimetry-derived estimates of ice shelf surface height [*Bamber et al.*, 2009] and from time series of satellite-based gravity measurements [*Ray et al.*, 2003]. The accuracy of tide models impacts directly upon the accuracy of such observations.

[1]School of Earth and Environment, University of Leeds, Leeds, UK.
[2]School of Geosciences, University of Edinburgh, Edinburgh, UK.

0148-0227/11/2011JC007294

[4] The waters around Antarctica present a challenge for tide models because (1) satellite altimeter observations commonly assimilated into models [*Egbert et al.*, 1994] do not extend to Antarctic coastal waters, (2) in situ tidal records are sparse [*King and Padman*, 2005], (3) ocean bathymetry is relatively uncertain, and (4) water column thickness beneath ice shelves is generally not well known. Consequently, tide models perform less well around Antarctica than at more northerly latitudes [*King and Padman*, 2005; *King et al.*, 2011]. Where in situ records exist, these can be used to evaluate tide models. However, large portions of the Antarctic coastline lack such records, and in these regions tide model accuracy is less certain. Satellite observations have been used to assess the accuracy of Antarctic tide models, including the techniques of laser altimetry [*Padman and Fricker*, 2005], radar altimetry [*Fricker and Padman*, 2002; *Shepherd and Peacock*, 2003] and InSAR [*Rignot et al.*, 2000; *Rignot*, 2002; *Padman et al.*, 2003a]. The utility of InSAR as a technique for measuring tidal motion was first demonstrated by *Hartl et al.* [1994] in a study of the Filchner-Ronne Ice Shelf. Later studies further developed this InSAR-based approach (1) to evaluate tide models at the Pine Island [*Rignot*, 2002] and Ross [*Padman et al.*, 2003a] ice shelves, (2) to demonstrate that InSAR could resolve small-scale tidal detail which was useful for model development [*Rignot et al.*, 2000], and (3) to describe a theoretical analysis of how individual tidal constituents could be determined from InSAR data [*Rignot et al.*, 2000].

[5] At present, tide model accuracy in the Amundsen Sea Sector of West Antarctica remains relatively uncertain. Only one study [*Rignot*, 2002] has performed an assessment of a tide model in this region, which forms part of a 75° arc of coastline lacking (as of 2005) any in situ tidal records [*King and Padman*, 2005]. InSAR-based studies hold the potential to evaluate tide models in this region. However, a comprehensive assessment of the errors affecting InSAR observations of ice shelf tidal motion has yet to be conducted. Here we investigate the utility of two interferometric methods for evaluating ocean tide models. We firstly quantify the measurement error associated with each interferometric method and then assess the accuracy with which three tide models are able to predict tidal motion of the Dotson Ice Shelf in the Amundsen Sea.

2. Theoretical Background

[6] The application of interferometric synthetic aperture radar to mapping ice motion has been well documented [*Goldstein et al.*, 1993; *Joughin et al.*, 1995, 1996a; *Kwok and Fahnestock*, 1996; *Rignot*, 1996]. Here, we provide only a short overview of the methods relevant to our study. InSAR provides a measurement of ground displacement that is of superior precision and spatial resolution to other remote sensing methods, such as synthetic aperture radar (SAR) intensity tracking [*Werner et al.*, 2001; *Massom and Lupin*, 2006]. It is however limited by its dependency upon surface coherence (i.e., the maintenance of a stable configuration of scatterers within each resolution cell). As such, it performs best over short time periods, typically measuring surface displacement over a period of several days. InSAR utilizes SAR image pairs to measure relative changes in the phase of the signal returned from a scattering surface. For any given pixel in a coregistered SAR image pair, the unwrapped interferometric phase difference, φ, is related to the difference in the pixel-to-satellite range, Δr, by

$$\varphi = \frac{4\pi}{\lambda}\Delta r, \tag{1}$$

where λ is the radar wavelength (~5.7 cm for the European Remote Sensing (ERS) satellites used in this study). For repeat pass SAR acquisitions, the interferometric phase signal, φ, consists of a linear combination of terms:

$$\varphi = \varphi_{flat} + \varphi_{topo} + \varphi_{displ}, \tag{2}$$

which refer to phase variations due to (1) increases in viewing angle across the ground track, φ_{flat} (as described by the shape of Earth's ellipsoid), (2) surface topography, φ_{topo}, and (3) surface displacement in the radar's line of sight (range) direction, φ_{displ}, which occurs between the two SAR acquisitions. For the remainder of this section we shall assume that the first two terms have been simulated from a digital elevation model (DEM) and knowledge of the satellites' spatial configuration, and removed from the interferometric phase in order to isolate the displacement term [e.g., *Joughin et al.*, 1998]. Errors associated with the incomplete removal of these effects will be assessed in section 6.

[7] When InSAR images a floating ice shelf, the surface displacement term, φ_{displ}, is commonly separated into steady and nonsteady components. Typically, the flow component of the displacement field due to ice moving downstream is categorized as a steady motion, approximately in the locally horizontal plane [*Goldstein et al.*, 1993; *Rignot*, 1996; *Rignot and MacAyeal*, 1998; *Rignot et al.*, 2000]. In contrast, the tidal component of motion, resulting from the oscillation of the floating ice shelf in response to the action of the ocean tide, is taken to be a vertical nonsteady motion. Additionally, over the time scales of the InSAR data used in this study, atmospheric pressure changes can cause variations in sea surface height of the order of 10 cm [*Rignot et al.*, 2000; *Padman et al.*, 2003b]. This atmospheric forcing introduces a further source of vertical nonsteady ice shelf motion. Because of the viewing angle of the satellites used in this study (~23° from vertical) the interferometer is at least 2.4 times more sensitive to vertical motion than to motion in the horizontal plane. The basis for this work is that the displacement component of the phase signal (φ_{displ}) may be characterized as a simple combination of these separate flow (φ_{flow}), tidal (φ_{tide}), and atmospheric pressure (φ_{press}) signals:

$$\varphi_{displ} = \varphi_{flow} + \varphi_{tide} + \varphi_{press}. \tag{3}$$

Here we describe two techniques that exploit differences in the temporal variability of these modes of displacement to separate the steady (flow) and nonsteady (tide plus atmospheric pressure) components of ice shelf motion. These techniques provide the basis for two methods of evaluating tide models; one which determines tidal displacement (i.e., the tide-induced change in ice shelf elevation) and the other which measures the difference between two displacements.

2.1. Single-Difference Approach

[8] Our first method follows a similar approach to that described by *Rignot* [1996]. We aim to directly estimate the

Table 1. Single-Difference Synthetic Aperture Radar Data[a]

Image Pair: Sensor-Orbit-Frame	Ice Shelf	Reference Image Acquisition	Image Pair Temporal Separation (days)	Track	$B_\perp$ (m)
		Interferometric Data			
e1-13153-5182, e1-13196-5182	Dotson	20 Jan 1994	3	39	17
e1-13239-5182, e1-13282-5182	Dotson	26 Jan 1994	3	39	−196
e1-13325-5182, e1-13368-5182	Dotson	1 Feb 1994	3	39	44
e1-13626-5182, e1-13669-5182	Dotson	22 Feb 1994	3	39	−23
e1-13798-5182, e1-13841-5182	Dotson	6 Mar 1994	3	39	−2
		Tracking Data			
e1-13153-5182, e1-13368-5182	Dotson	20 Jan 1994	15	39	

[a]Here e1 signifies the ERS-1 satellite. $B_\perp$ specifies the perpendicular baseline of the interferometer.

nonsteady, vertical displacement of the ice shelf, Δz, captured within a single interferogram. This method measures the difference in the ice shelf height between the times of the two SAR acquisitions and so we refer to it as a single-difference technique.

[9] First we estimate the flow component of the line of sight displacement recorded by an interferogram, Δr_{flow}. This flow signal is extracted from a 2-D map of ice flow, which is determined by tracking the displacement of surface features in pairs of SAR backscatter intensity images. Because this tracking method measures displacement over a relatively long time period (see Table 1 for details) it is insensitive to short-period signals and provides a close approximation of the steady flow signal. We then scale this tracking-derived displacement so that it matches the time scale of the interferogram. To isolate the nonsteady signal within an interferogram, we convert the interferometric phase into a line of sight displacement (equation (1)), remove the tracking-derived flow component, and convert the remaining nonsteady signal into a vertical displacement:

$$\Delta z_{tide} + \Delta z_{press} = \frac{\Delta r - \Delta r_{flow}}{\cos\psi}. \tag{4}$$

Here ψ is the incidence angle of the radar beam relative to the normal to Earth's ellipsoid, and Δz_{tide} and Δz_{press} denote the vertical change in ice shelf height occurring during the acquisition of the interferogram because of the tide and atmospheric pressure fluctuations. To isolate the tidal component of this nonsteady vertical motion, we use an inverse barometer approximation to correct for the effect of change in atmospheric pressure [*Padman et al.*, 2003b]. This single-difference method assumes that the average velocity recorded within an interferogram matches that of the velocity observed using our tracking technique (see Table 1 for a description of the acquisition periods of these techniques). Otherwise the tracking result will not exactly cancel the flow component of the interferometric signal. The single-difference technique is further limited by its reliance upon the SAR intensity tracking technique, which has an inferior precision and resolution to InSAR [*Werner et al.*, 2000].

2.2. Double-Difference Approach

[10] Our second method follows earlier work [*Hartl et al.*, 1994; *Rignot*, 1996, 2002], whereby two interferograms are differenced in order to cancel the displacement component of the interferometric phase common to both interferograms. If flow velocities remain constant during the acquisition period, then the remaining phase signal describes the difference in the vertical motion recorded in the two interferograms:

$$\Delta z_{1,tide} - \Delta z_{2,tide} + \Delta z_{1,press} - \Delta z_{2,press} = \frac{\lambda}{4\pi\cos\psi}\left(\varphi_{1,displ} - \varphi_{2,displ}\right), \tag{5}$$

where the subscripts 1 and 2 refer to the first and second interferograms. As with the single-difference technique, an inverse barometer correction is applied to isolate the tidal signal. The resulting tidal signal is the difference between the two height differences captured in the pair of interferograms, and we therefore refer to this method as a double-difference technique. This method assumes that identical displacement occurs during each of the interferogram acquisitions. It also, by its nature, requires greater quantities of coherent SAR data.

3. Study Area

[11] In this study we focus upon the Dotson Ice Shelf in the Amundsen Sea sector of the West Antarctic Ice Sheet (WAIS) (Figure 1). Holding enough ice to raise sea levels by ~1.5 m, the Amundsen Sea sector of the WAIS has the greatest mass deficit of all of Antarctica [*Rignot et al.*, 2008]. Over the last two decades, satellite observations of this region have revealed a pattern of thinning of both grounded [*Shepherd et al.*, 2002; *Pritchard et al.*, 2009; *Wingham et al.*, 2009] and floating [*Shepherd et al.*, 2004; *Wingham et al.*, 2009] ice, glacier acceleration [*Rignot*, 2008] and grounding line retreat [*Rignot*, 1998]. The penetration of warm circumpolar deep water via seabed troughs [*Nitsche et al.*, 2007; *McMillan et al.*, 2009] to sub–ice shelf cavities [*Thoma et al.*, 2008; *Jenkins et al.*, 2010] suggests that high rates of ice shelf basal melting [*Rignot and Jacobs*, 2002; *Shepherd et al.*, 2004] are primarily responsible for the changes witnessed in this region [*Payne et al.*, 2007].

[12] The Dotson Ice Shelf (Figure 1) occupies an area of ~3400 km^2 and is ~450 m thick [*Shepherd et al.*, 2004]. It is fed by the Smith and Kohler Glaciers, which over recent decades have suffered sustained net mass loss [*Rignot*, 2006]. Close to the grounding line of the Dotson Ice Shelf, grounded ice has been thinning for the past 20 years, at a mean rate that exceeds 1.5 m/yr [*Shepherd et al.*, 2002; *Pritchard et al.*, 2009]. Between 1992 and 2001, satellite altimeter observations of ice shelf surface lowering indicated that the ice shelf thinned at an average rate of 3.3 ± 0.4 m/yr [*Shepherd et al.*, 2004]. By assessing the contributions from the various processes affecting surface lowering (namely, temporal

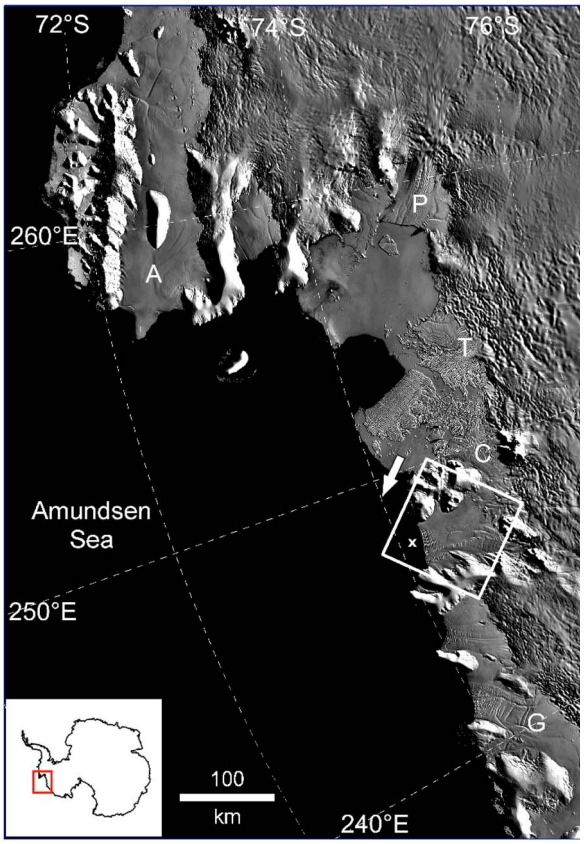

Figure 1. The Dotson Ice Shelf, West Antarctica. Thick white outline indicates synthetic aperture radar (SAR) data coverage over the Dotson Ice Shelf, and the white arrow indicates the across-track (ground range) direction of the satellite. A white cross indicates the location where tide model data were extracted for model evaluation. A, Abbot Ice Shelf; P, Pine Island Ice Shelf; T, Thwaites Ice Shelf; C, Crosson Ice Shelf; G, Getz Ice Shelf. Background image is taken from the Moderate Resolution Imaging Spectroradiometer (MODIS) mosaic of Antarctica [*Haran et al.*, 2005].

fluctuations in sea level height, ocean density, ice shelf density, surface mass accumulation, and ice mass flux divergence), *Shepherd et al.* [2004] estimated an average net basal melt rate underneath the Dotson Ice Shelf of ~8 m/yr.

4. Data

4.1. Interferometric Synthetic Aperture Radar

[13] In this study we used SAR data acquired by the European Remote Sensing satellites (ERS-1/2) to determine ice shelf motion. The SAR data were acquired during the first and second ice phases of ERS-1 (during early 1992 and early 1994, respectively), and the ERS-1/2 tandem phase (1995–1996) (Tables 1 and 2). The SAR data were acquired in raw format and processed using the Gamma software package [*Werner et al.*, 2000]. We used a 5 km Antarctic-wide DEM [*Bamber and Bindschadler*, 1997] to simulate and remove the topographic component of the interferometric phase. The effect of DEM inaccuracies is considered in section 6.

4.2. Tide Models

[14] We used three tide models to simulate the effect of ocean tides on the InSAR observations: the Circum-Antarctic Tidal Simulation, Inverse Model Version 2008a (CATS2008a_opt), TPXO7.1 [*Egbert and Erofeeva*, 2002] and the Finite Element Solution model FES2004 [*Lyard et al.*, 2006] (hereafter referred to as CATS, TPXO and FES). CATS is an updated version of the regional inverse model described by *Padman et al.* [2002]. These models (or their predecessors, CATS02.01 and TPXO6.2) are among the most accurate around Antarctica, with root-mean-square errors of 6–17 cm based on a comparison with tidal records (four major tidal constituents only) [*King and Padman*, 2005].

[15] The tide models considered here are built on different-sized grids. FES and TPXO are both global tide models, with 1/8° and 1/4° resolution, respectively (equating to a resolution of the order of tens of kilometers at the latitude of this study). CATS is a high-resolution regional model, for the waters around Antarctica only, and operates at a 4 km grid spacing. All 3 models assimilate remotely sensed and ground-based data in order to constrain their physical forward model. FES utilizes sparse Antarctic tide gauge data (less than 10 records), along with TOPEX/Poseidon and ERS altimetry. TPXO assimilates TOPEX/Poseidon and TOPEX tandem

Table 2. Double-Difference Synthetic Aperture Radar Data[a]

Image Pairs: Sensor-Orbit-Frame	Ice Shelf	Reference Image Acquisition	Image Pair Temporal Separation (days)	Track	$B_\perp$ (m)
e1-03318-5182, e1-03361-5182	Dotson	4 Mar 1992	3	39	
& e1-03404-5182, e1-03447-5182	Dotson	10 Mar 1992	3	39	57
e1-13153-5182, e1-13196-5182	Dotson	20 Jan 1994	3	39	
& e1-13196-5182, e1-13239-5182	Dotson	23 Jan 1994	3	39	82
e1-13153-5182, e1-13196-5182	Dotson	20 Jan 1994	3	39	
& e1-13239-5182, e1-13282-5182	Dotson	26 Jan 1994	3	39	214
e1-22400-5176, e2-02727-5176	Dotson	27 Oct 1995	1	368	
& e1-24404-5176, e2-04731-5176	Dotson	15 Mar 1996	1	368	141
e1-23817-5175-5193, e2-04144-5175-5193	Dotson	3 Feb 1996	1	282	
& e1-24318-5175-5193, e2-04645-5175-5193	Dotson	9 Mar 1996	1	282	39
e1-23885-5601, e2-04212-5601	Crosson	8 Feb 1996	1	350	
& e1-24386-5601, e2-04713-5601	Crosson	14 Mar 1996	1	350	−80

[a]Here e1 and e2 signify the ERS-1 and ERS-2 satellites. $B_\perp$ specifies the effective perpendicular baseline and is calculated as the difference between the perpendicular baselines of the two component interferograms.

radar altimetry, and Antarctic tide gauge data. CATS is forced by tide heights from TPXO at its northern boundary, and assimilates TOPEX/Poseidon altimetry, ~50 tidal records and ICESat laser altimetry from the Ross and Filchner-Ronne ice shelves. We used the load tide model TPXO6.2_load [*Egbert and Erofeeva*, 2002] to correct CATS and TPXO for the ocean floor deformation associated with the tidal displacement of water (this correction is included within FES).

4.3. Meteorological Model Reanalysis

[16] To account for ice shelf height changes arising from atmospheric pressure fluctuations we used surface level atmospheric pressure data from the European Centre for Medium-Range Weather Forecasts' (ECMWF) ERA-40 reanalysis [*Uppala et al.*, 2005]. These data were acquired from the British Atmospheric Data Centre on a 1° × 1° regularly spaced grid, which was derived from an N80 reduced Gaussian grid. ERA-40 provides surface pressure fields at 6-hourly intervals and so we used a linear interpolation between the two closest times to derive pressure estimates at the times of SAR data acquisition.

5. Methods

[17] In this section we describe the practical application of the theoretical approach outlined in section 2. We begin by detailing the processing steps of our single-difference and double-difference techniques. We then describe how we compare our results to tide model predictions.

5.1. Single-Difference Technique

[18] We formed multiple interferograms from coregistered SAR image pairs (Table 1), and then used estimates of surface displacement determined using SAR intensity tracking to approximate, and remove, the flow signal recorded within each interferogram (equation (4)). A similar method was used by *Rignot* [1996], who used 11 velocity estimates (determined by tracking a set of crevasses) to estimate tidal displacement at the Petermann Ice Shelf, Greenland. In sections 5.1.1–5.1.3 we describe the main stages of this process.

5.1.1. SAR Intensity Tracking

[19] Previous studies [*Werner et al.*, 2001; *Strozzi et al.*, 2002; *Luckman et al.*, 2003] have demonstrated that surface displacement can be mapped from a pair of coregistered SAR backscatter intensity images, by tracking the motion of features in the two images. The data processing can be divided into two main stages; image coregistration and displacement mapping. In the first step, images must be accurately coregistered, in order to minimize the misinterpretation of image coregistration errors as surface displacement. In the second step, small subsections (also known as patches) of the two images are matched in order to determine displacement offsets.

[20] Both image coregistration and the estimation of surface displacement utilize the same cross-correlation technique, and so care must be taken in the coregistration step to avoid mistakenly accounting for a component of the surface displacement field. In situations where major sections of the imaged area are stationary during the acquisition period, accurate coregistration can be achieved by estimating the offsets of large-scale features over the entire image, and culling anomalous values which may include ice motion [*Pritchard et al.*, 2005]. However, only a small proportion of our study area exhibits such stability, with the majority of the imaged area consisting of moving ice or ocean. We therefore applied a mask prior to coregistration so that coregistration was based solely on nonmoving areas. Because these areas were not extensive, we based our coregistration upon offsets compiled from two patch sizes, enabling us to exploit a range of different sized features and increase the number (214) of offsets used. Bilinear functions of range and azimuth pixel number were fitted to these offset estimates in order to perform image coregistration. We chose not to fit a higher-order polynomial because (1) the data points used to determine the polynomial were limited in extent and irregular in distribution, and (2) a first-order polynomial is sufficient to represent the principle transformations required to coregister ERS data (namely, image shifts, stretches and small rotations).

[21] Once images were coregistered, we performed SAR intensity tracking to produce a displacement map with a nominal pixel spacing of ~240 × 200 m. To determine displacement, we cross-correlated patches with dimensions of 128 pixels in range and 512 pixels in azimuth (~2.6 × 2.0 km in ground coordinates). Tracking features of this size maximized the area over which a coherent displacement signal was retrieved. Finally, a mask was applied to regions where high-frequency noise dominated the displacement signal. During the ice phase of the ERS-1 mission, images of the Dotson Ice Shelf were acquired at regular 3 day intervals, allowing us to form a series of displacement maps from image pairs acquired over a range of time scales. From these data, we selected the optimal image pair (Table 1, 15 day separation) on the basis of the two desirable criteria of maximizing the area over which we obtained a coherent displacement signal, and minimizing displacement offsets over stationary areas.

5.1.2. InSAR

[22] Taking each interferogram, we firstly isolated the displacement component of the interferometric signal (equation (2)). The simulated topographic component, together with the phase signal originating from the changing look angle across the satellite track (the flat Earth signal), was projected into the SAR imaging geometry and removed from each interferogram. During the simulation of the topographic and flat-Earth phase signals, we used precise orbit information acquired from the Technical University of Delft to determine the imaging geometry. Further baseline refinement was not necessary for our study because we only use image-wide averages of relative displacement (see section 6 for a further discussion and assessment of the associated error). Each interferogram was smoothed, unwrapped [*Goldstein et al.*, 1988] and converted to a map of displacement in the range direction. The InSAR map shows only relative displacement, i.e., how displacement varies across the image. To convert to absolute displacement, these relative displacement values were tied down to pixels with known displacement. Commonly, nonmoving regions of the image are identified, such as bedrock protruding though the ice or areas of known stagnant flow. These must be linked to the ice shelf by a path that does not cross discontinuities in the interferometric phase. Because we were not confident that we could identify such a path we did not tie down our InSAR displacement

Table 3. Summary of Error Terms[a]

Error Term	Single-Difference Error (cm)	Double-Difference Error (cm)
Topography, ε_{topo}	0.1	0.2
Flat-Earth correction, ε_{flat}	0.8	1.1
Flow, ε_{flow}	6.5	0
Atmospheric pressure, ε_{press}	1.4	2.0
Atmospheric distortion, ε_{atm}	1.9	2.7
Coherence, ε_{coh}	0.1	0.2
Unwrapping, ε_{unw}	0	0
Total, ε	7.0	3.5

[a]Each term is the average calculated from all interferograms used by that technique.

maps to stationary regions. Instead we used range displacement values derived using SAR intensity tracking, at locations where ice was grounded, to provide ~2400 points of known velocity to tie down each InSAR map.

5.1.3. Removing the Ice Flow Signal

[23] We used the velocities derived by SAR intensity tracking to remove the flow component of the displacement signal from each InSAR displacement map. Because InSAR only measures changes in the satellite's line of sight (range) direction, we used only the component of the tracking displacement in that direction. Differencing each InSAR-derived displacement map and the range component of the SAR intensity tracking displacement map isolated nonsteady displacement. This displacement was converted into a vertical motion.

5.2. Double-Difference Technique

[24] We formed multiple interferograms from coregistered SAR image pairs (Table 2), and then differenced pairs of interferograms to isolate the nonsteady component of the displacement signal. The procedure outlined in section 5.1 was followed to remove topographic and flat-Earth effects, and convert the differenced interferograms to a vertical displacement map.

5.3. Tide Model Evaluation

[25] Tide heights were determined from each of the three tide models at the times of the SAR data acquisitions, at a location just seaward of the ice front (74.1°S, 247.5°E, marked in Figure 1). We did not use model predictions coincident with the ice shelf itself because of inconsistencies between the models at those locations (see section 8.2). These predictions were combined so as to give estimates of the tidal signal, as recorded by our single- and double-difference methods. In a similar way, equivalent predictions of the atmospheric pressure signals were formed from the model reanalysis data. These were converted to ice shelf height changes assuming an inverted barometer response at a rate of −0.95 cm/hPa, which was determined empirically by *Padman et al.* [2003b]. These estimates were used to account for ice shelf motion arising from atmospheric pressure fluctuations. The observed mean tidal displacements over the freely floating portion of the ice shelf were then compared to the tide model predictions. For this comparison, we considered only the mean tidal displacement in order to reduce the effect of measurement error (section 6). This step sacrifices spatial resolution but allows us to derive a single estimate of tidal displacement with which to characterize each data set.

6. Error Assessment of Single-Difference and Double-Difference Methods

[26] To assess the certainty with which InSAR data can be used to evaluate tide models, and the relative strengths of our two InSAR-based methods, we considered the ability of our methods to completely remove all other signals. We define the error associated with each observation of tide as follows:

$$\varepsilon^2 = \varepsilon_{topo}^2 + \varepsilon_{flat}^2 + \varepsilon_{flow}^2 + \varepsilon_{press}^2 + \varepsilon_{atm}^2 + \varepsilon_{coh}^2 + \varepsilon_{unw}^2, \quad (6)$$

where ε_{topo}, ε_{flat}, ε_{flow}, and ε_{press} are the errors associated with the incomplete removal of terms in equations (2) and (3), ε_{atm} is the error arising from atmospheric distortions of the phase signal, ε_{coh} is the error due to loss of signal coherence between the radar acquisitions and ε_{unw} arises from any error in the unwrapping process. In this section we estimate the magnitude of each of these components; a summary of these error terms is provided in Table 3. The errors quoted are the mean values obtained from the data sets used to evaluate each component.

6.1. Topographic Error

[27] In this study we have used a DEM to remove the topographic component of the interferometric phase. Spurious topographic phase signals, which will be falsely interpreted as surface displacement, arise from inaccuracies in both the DEM and the baseline estimation (the latter effect causing an incorrect scaling of the DEM when removing the topographic phase). The following analysis of these error terms is based on the work of *Joughin et al.* [1996a]. We resolve the baseline, B, into components perpendicular, $B_\perp$, and parallel, $B_\parallel$, to the radar's center look direction, θ_c. The sensitivity of the interferometric phase to topography can be approximated [*Joughin et al.*, 1996a] as

$$\varphi_{topo} = \frac{4\pi B_\perp}{\lambda r \sin\theta_c} z, \quad (7)$$

where r denotes the range from the satellite to the target pixel, and z the elevation of the target pixel above Earth's ellipsoid. If z is determined from a DEM, with an associated error ε_z, then the corresponding error in the interferometric phase will be given by

$$\varepsilon_z^\varphi = \frac{4\pi B_\perp}{\lambda r \sin\theta_c} \varepsilon_z. \quad (8)$$

[28] Falsely interpreting this topographic phase error as a surface displacement in the satellite's line of sight direction, and converting to a vertical tidal motion yields

$$\varepsilon_z^{\Delta z} = \frac{B_\perp}{r \sin\theta_c \cos\psi} \varepsilon_z, \quad (9)$$

where ψ is the incidence angle of the radar beam relative to the normal to Earth's ellipsoid. Taking typical values for the ERS satellites for θ_c, ψ, and r of 23°, 26°, and 862.5 km respectively, and a DEM error of 5 m [*Bamber and Gomez-Dans*, 2005] on the basis of the average surface slope of ice

in our study area gives the vertical displacement error arising from our DEM as a function of perpendicular baseline:

$$\varepsilon_z^{\Delta z} = 1.65 \times 10^{-5}\, B_\perp. \tag{10}$$

This yields mean vertical displacement errors, resulting from DEM inaccuracies, of 0.1 cm and 0.2 cm for our single-difference and double-difference data sets, respectively.

[29] To determine the effect of the second form of topographic error, that of inappropriate scaling of the topographic phase, we rewrite equation (9) as a function of the perpendicular baseline error:

$$\varepsilon_{B_\perp}^{\Delta z} = \frac{z}{r \sin\theta_c \cos\psi}\varepsilon_{B_\perp}. \tag{11}$$

We assume the geographically noncorrelated components of the across-track and radial precision orbit errors to be 8 and 5 cm, respectively [*Hanssen*, 2001]. On the basis of the satellite geometry, we project this error vector into the perpendicular baseline direction to determine a 9 cm orbital error in that direction, and a $\sqrt{2} \times 9 = 13$ cm perpendicular baseline error. Using the ERS orbit parameters outlined above, and a mean ice elevation (determined from the DEM) in our study region of 75 m, we estimate $\varepsilon_{B_\perp}^{\Delta z}$ as 2×10^{-3} cm, which is insignificant in comparison to the topographic error resulting from DEM inaccuracies. Combining the two sources of topographic error gives mean single-difference and double-difference errors of 0.1 and 0.2 cm, respectively. The topographic error is small because of the minimal relief of the ice surface at our study site.

6.2. Flat-Earth Correction Error

[30] Errors in removing the flat-Earth phase signal arise from inaccuracies in estimating the interferometric baseline. Here we start with the approximation determined by *Joughin et al.* [1996a] from the interferometric geometry:

$$\varepsilon_{flat}^{\varphi} = \frac{4\pi}{\lambda}\left(\varepsilon_{B_\perp} \sin\theta_{d,flat} + \varepsilon_{B_\parallel} \cos\theta_{d,flat}\right), \tag{12}$$

where $\varepsilon_{\text{flat}}^{\varphi}$ is the flat Earth phase error, $\varepsilon_{B_\perp}$ and $\varepsilon_{B_\parallel}$ are the errors in estimating the perpendicular and parallel components of the baseline, and $\theta_{d,flat}$ is the angular deviation from the center of the radar beam across the image swath, assuming no topography. Two factors are important here: (1) we measure the displacement of floating ice relative to grounded ice, and (2) to mitigate the effect of the perpendicular baseline error, we have taken spatial averages over each of the grounded and floating regions of ice to determine a single estimate of tidal displacement at each epoch. Consequently, the displacement error resulting from unmodeled baseline effects is determined by the change in the mean baseline error estimated over the grounded and floating regions of ice. Across the image track, the parallel baseline error term remains effectively constant, and so will not contribute to $\varepsilon_{\text{flat}}^{\varphi}$. The perpendicular baseline error term contributes an almost linear phase ramp across the image swath, with zero error at the center line of the swath ($\theta_{d,flat} = 0$). Consequently, the contribution of this term to our total error will be determined by the phase change associated with this ramp, occurring between grounded and floating regions. From these considerations we ignore the parallel baseline term and rewrite equation (12) as

$$\varepsilon_{flat}^{\varphi} = \frac{4\pi}{\lambda}\varepsilon_{B_\perp} \sin\left(\langle\theta_{d,fl}\rangle - \langle\theta_{d,gr}\rangle\right), \tag{13}$$

where $\langle\theta_{d,fl}\rangle$ and $\langle\theta_{d,gr}\rangle$ are the mean angular deviations of floating and grounded ice regions, respectively. Over our study area, $\langle\theta_{d,fl}\rangle - \langle\theta_{d,gr}\rangle = 3.2°$.

[31] As before (section 6.1), we assume a 13 cm error in our perpendicular baseline estimate, which equates to a $\sqrt{2} \times 13 = 18$ cm error in our double-difference baseline estimates. Applying equation (13), and converting to a vertical displacement, yields flat Earth errors of 0.8 and 1.1 cm for our single-difference and double-difference approaches, respectively.

6.3. Ice Flow Error

6.3.1. Single-Difference Method

[32] As part of our single-difference method, we removed the flow component of the interferometric signal using estimates determined from SAR intensity tracking. Errors in canceling the flow signal may arise from errors in our tracking displacement map. Specifically, high-frequency noise may arise from inaccuracies in matching image patches using the intensity tracking technique, and errors in the SAR image pair coregistration may contribute long-wavelength errors. In this study we mitigate the effect of high-frequency noise by spatially averaging displacement estimates over the ice shelf. However, long-wavelength coregistration errors in our tracking estimates will contribute a spurious signal to our estimates of single-difference tidal displacement. We estimate this error, $\varepsilon_{flow}^{\Delta z}$, by converting to a vertical displacement the mean line-of-sight displacement of ~9500 pixels which are located on stable ground:

$$\varepsilon_{flow}^{\Delta z} = \frac{\langle\Delta r_{stable}\rangle}{\cos\psi}, \tag{14}$$

where $\langle\Delta r_{stable}\rangle$ denotes the mean line-of-sight displacement of stable pixels and ψ is the incidence angle of the radar beam. From this calculation we determine a 6 cm ice flow error in our single-difference measurements of vertical tidal displacement. Incomplete cancellation of the flow signal may also arise from flow variations occurring during the different length sampling periods (3 days for InSAR versus 15 days for tracking). Without independent high-quality velocity measurements (e.g., from in situ Global Positioning System data) we cannot directly quantify this effect. However, we have aimed to minimize any influence by (1) forming InSAR and SAR intensity tracking predictions from contemporaneous data, and (2) measuring displacement relative to grounded ice (which will undergo similar variations in flow to that of the ice shelf itself).

6.3.2. Double-Difference Method

[33] We do not utilize velocities determined from SAR intensity tracking when estimating tidal motion using the double-difference approach, and so the only source of ice flow errors are those that may potentially arise from nonsteady variations in flow. Specifically, errors in our double-difference tidal predictions could arise if the total displacement occurring during an interferogram acquisition (i.e., 1 or 3 day displacement) varies between the first and second

interferograms. To investigate the prevalence of such a signal, we checked our double-difference displacement maps for long-wavelength displacement variation indicative of a residual flow signal. Spatial variation in displacement over the ice shelf was small (~1 cm on average for our data set), indicating no significant residual flow signal. We therefore discount this term in our double-difference error budget.

6.4. Atmospheric Pressure Error

[34] Incomplete removal of ice shelf height changes associated with atmospheric pressure fluctuations will result from inaccuracies in model predictions of atmospheric pressure, and in particular from a failure to predict the timing of large pressure fluctuations associated with passing weather fronts [*Padman et al.*, 2003b]. The scarcity of independent in situ meteorological records in remote regions such as the Amundsen Sea limits the assessment of the accuracy of the model reanalysis upon which our atmospheric pressure correction is based. However, one study [*King*, 2003] has performed an evaluation of the ECMWF modeled surface level atmospheric pressure in the nearby Bellingshausen Sea on the basis of independent field data. Although these data span only a relatively short period (February–May 2001), they agree well with the model predictions. We take the 1.05 hPa standard deviation of the model predictions from the independent observations [*King*, 2003] as an estimate of the error associated with each model estimate of atmospheric pressure. We then calculate the corresponding error associated with single- and double-difference pressure estimates, and convert these to errors in vertical displacement using the empirical ratio determined by *Padman et al.* [2003b]. This yields errors associated with our inverse barometer correction of 1.4 and 2.0 cm in our single- and double-difference estimates of tidal motion, respectively.

[35] A second source of error associated with our correction for atmospheric pressure fluctuations arises from the validity of the inverse barometer approximation as a means for converting from pressure to ice shelf height changes. Previous studies [*Ponte et al.*, 1991; *Padman et al.*, 2003b] have shown the inverse barometer approximation to be valid at frequencies lower than ~0.5 cycles per day (cpd). At these frequencies the ocean responds to changes in atmospheric pressure such that equilibrium is maintained. Consequently, pressure changes correlate well with sea surface height changes. The repeat times of our satellite observations (Tables 1 and 2) require that we model this effect at 0.3 and 1.0 cpd, and so we are at limit of the frequency range at which an inverse barometer approximation is valid. As such, it is possible that this correction does not account for the full spectrum of atmospheric pressure-driven height changes, in particular for our double-difference approach which utilizes some 1 day repeat data (Table 2). In section 8.3 we further investigate our inverse barometer correction, to determine whether, in light of these limitations, such an approximation is beneficial in reducing atmospheric pressure-related signals.

6.5. Atmospheric Distortions

[36] The two primary sources of atmospheric distortions affecting repeat pass interferometry arise from tropospheric delay and ionospheric disturbances. Spatial and temporal tropospheric inhomogeneity causes varying phase delays in the radar signal [*Goldstein*, 1995; *Massonnet and Feigl*, 1998], primarily as a result of changing water vapor content. On the basis of Global Positioning System data, the effect of the varying state of the troposphere on interferometric measurements has been parametrized [*Emardson et al.*, 2003] over a range of length and time scales by

$$\varepsilon_{tropo}^{\Delta r} = cL^{\alpha} + kH, \tag{15}$$

where $\varepsilon_{tropo}^{\Delta r}$ is the line-of-sight displacement error due to tropospheric effects (in mm), c and α vary according to the time scale of the acquisition, and L and H are the length scale and height difference, respectively (in km), over which tropospheric variability is estimated. Over the scales relevant to our study (50 km length scale, 0.1 km height difference, and 3 day time period (corresponding to $c = 2.6$, $\alpha = 0.48$, $k = 3.4$ [*Emardson et al.*, 2003])), equation (15) gives tropospheric errors in our single-difference and double-difference estimates of vertical displacement of 1.9 and 2.7 cm, respectively. These estimates can be taken as an upper bound for tropospheric error because, in comparison to the Californian study site of *Emardson et al.* [2003], Antarctic tropospheric water vapor variability, and hence, c is likely to be much reduced [*Trenberth et al.*, 2005].

[37] Over the spatial and temporal interval for which a SAR illuminates a target, variations in the density of electrons in the ionosphere can modulate the phase signal [*Gray et al.*, 2000] and cause errors in associated displacement measurements. This effect can manifest itself as distinctive azimuth streaks in the azimuth component of the coregistration offsets, the coherence image and the interferogram [*Joughin et al.*, 1996b; *Mattar and Gray*, 2002]. We checked each interferogram, its corresponding coherence image and the azimuth component of our tracking solution and found no evidence of such features. Furthermore, we note that (1) at the wavelength of ERS, ionospheric errors are typically subcentimeter [*Mattar and Gray*, 2002] and (2) by our spatial averaging we will further minimize any ionosphere effects. Consequently, we do not anticipate any significant ionospheric error in our displacement estimates, and so we disregard this term.

6.6. Coherence Error

[38] Interferometric phase errors arise from changes in surface properties occurring between the two SAR acquisitions [*Zebker and Villasenor*, 1992]. For a sufficiently multilooked image, the corresponding line of sight error, $\varepsilon_{coh}^{\Delta r}$, can be approximated [*Rodriguez and Martin*, 1992] from an estimate of the local coherence, γ, of the interferometric phase within each multilooked pixel:

$$\varepsilon_{coh}^{\Delta r} = \frac{\lambda}{4\pi\sqrt{2N}} \frac{\sqrt{1-\gamma^2}}{\gamma}, \tag{16}$$

where N is the number of looks that are averaged. For each interferogram, we take the spatial mean of $\varepsilon_{coh}^{\Delta r}$ as a measure of this error term. Converting to a vertical displacement yields mean errors of 0.1 cm for our single-difference approach and 0.2 cm for our double-difference approach.

6.7. Phase Unwrapping Error

[39] Errors can occur during the process of phase unwrapping when discontinuities in the interferometric phase

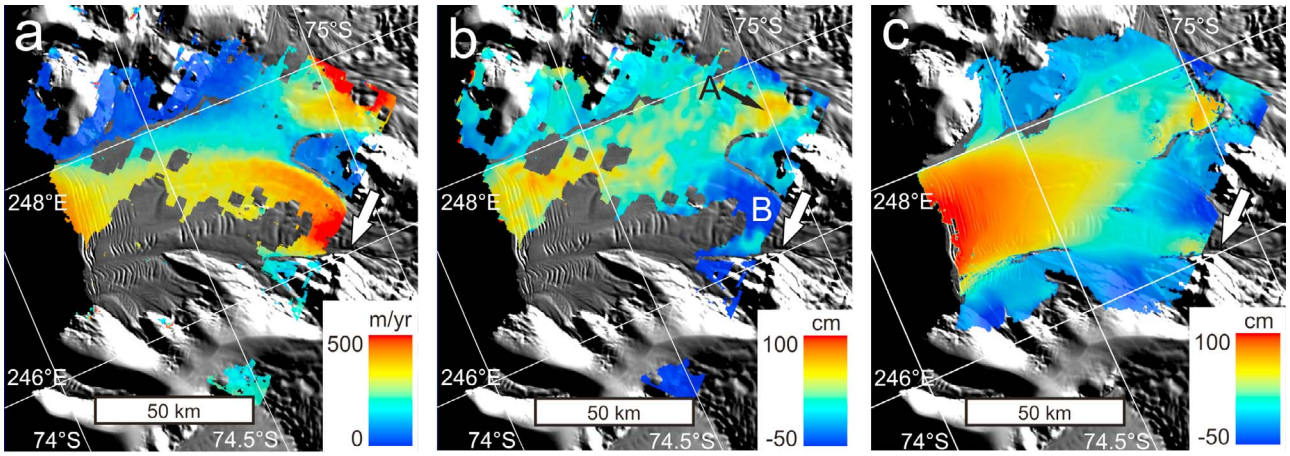

Figure 2. Displacement maps of the Dotson Ice Shelf. (a) Ice flow velocity determined using SAR intensity tracking (see Table 1 for data used). (b) Satellite line-of-sight (range) component of 3 day flow displacement, determined using SAR intensity tracking. (c) The 3 day line of sight (range) displacement from interferometric synthetic aperture radar (InSAR) (including both flow and tidal motion of the ice shelf). White arrows indicate the across-track (ground range) direction; A and B mark fast flowing features referred to in text. Background image is taken from the MODIS mosaic of Antarctica [*Haran et al.*, 2005].

(arising from noise or high phase gradients) are crossed [*Goldstein et al.*, 1988]. We checked each unwrapped interferogram to ensure that there was no evidence of the discontinuities associated with unwrapping error, and consequently we assumed no unwrapping errors to be present in our displacement maps.

6.8. Combined Error

[40] A summary of the relative contribution of the component error terms is given in Table 3. Assuming the tropospheric error to be at its upper bound, and combining error terms (equation (6)) yields estimated errors of 7.0 and 3.5 cm in our single- and double-difference estimates of vertical tidal displacement, respectively. Consequently, the double-difference technique provides a more accurate assessment of tide model accuracy, primarily because the method is independent of displacement estimates derived using SAR intensity tracking.

7. Results

[41] In this section we first describe our SAR observations of the flow velocity and tidal displacement of the Dotson Ice Shelf. We then use our observations of tidal motion to evaluate the FES, TPX and CATS tide models.

7.1. Observations of Ice Shelf Flow Displacement

[42] We have used the technique of SAR intensity tracking to estimate flow speeds across the Dotson Ice Shelf (Figure 2a). Although this map provides only partial coverage, it is sufficiently complete to determine that the ice shelf is fed by fast flowing ice from the southwest, which originates from the Smith and Kohler glaciers. Considerable flow variation exists over the ice shelf with velocities exceeding 500 m/yr close to the grounding line, yet falling to ~100 m/yr at other locations on the ice shelf. The range component of the tracking-derived ice velocities are required to isolate the tidal signal using the single-difference technique. These are shown in Figure 2b. In comparison to the range displacement map derived from InSAR (Figure 2c, which also includes vertical displacement), the SAR intensity tracking map offers more limited coverage and, because of its inferior resolution and precision, a noisier picture of range displacement. It may have been possible to derive a more spatially complete tracking displacement map, using data from an alternative epoch. However, for the purposes of our study, the priority was to obtain a solution contemporaneous with our InSAR data so as to minimize the impact of temporal variations in flow, and complete coverage of the ice shelf was not necessary. A qualitative comparison of the range component of the tracking displacements and the InSAR-derived displacements shows similar large-scale flow displacement patterns. Both resolve the same fast flowing features (marked A and B in Figure 2b), and a general pattern of increasing displacement toward the calving front of the ice shelf.

7.2. Observations of Ice Shelf Tidal Displacement

[43] We made observations of the tidal motion of the Dotson Ice Shelf at multiple epochs using our single-difference and double-difference techniques. We formed five maps of tidal displacement (e.g., Figure 3a) using our single-difference technique. These tidal predictions offer only partial coverage of the ice shelf, a consequence of the limited extent of our displacement map derived using SAR intensity tracking. The single-difference tidal maps exhibit substantial long- and short-wavelength variation, and visually this makes the distinction between floating and grounded ice unclear. There is a long-wavelength ramp in each of the five tidal predictions, leading to ~1 m variation in the tidal signal across the ice shelf. We discuss the origin of this ramp in section 8.1.

[44] We used 24 SAR images (Table 2) to form six maps of tidal motion (e.g., Figure 3b) using the double-difference technique. These predictions gave excellent spatial coverage and, in contrast to the single-difference technique, resolved a detailed pattern of floating and grounded ice (blue and red colors, respectively, in Figure 3b). These solutions indicate a

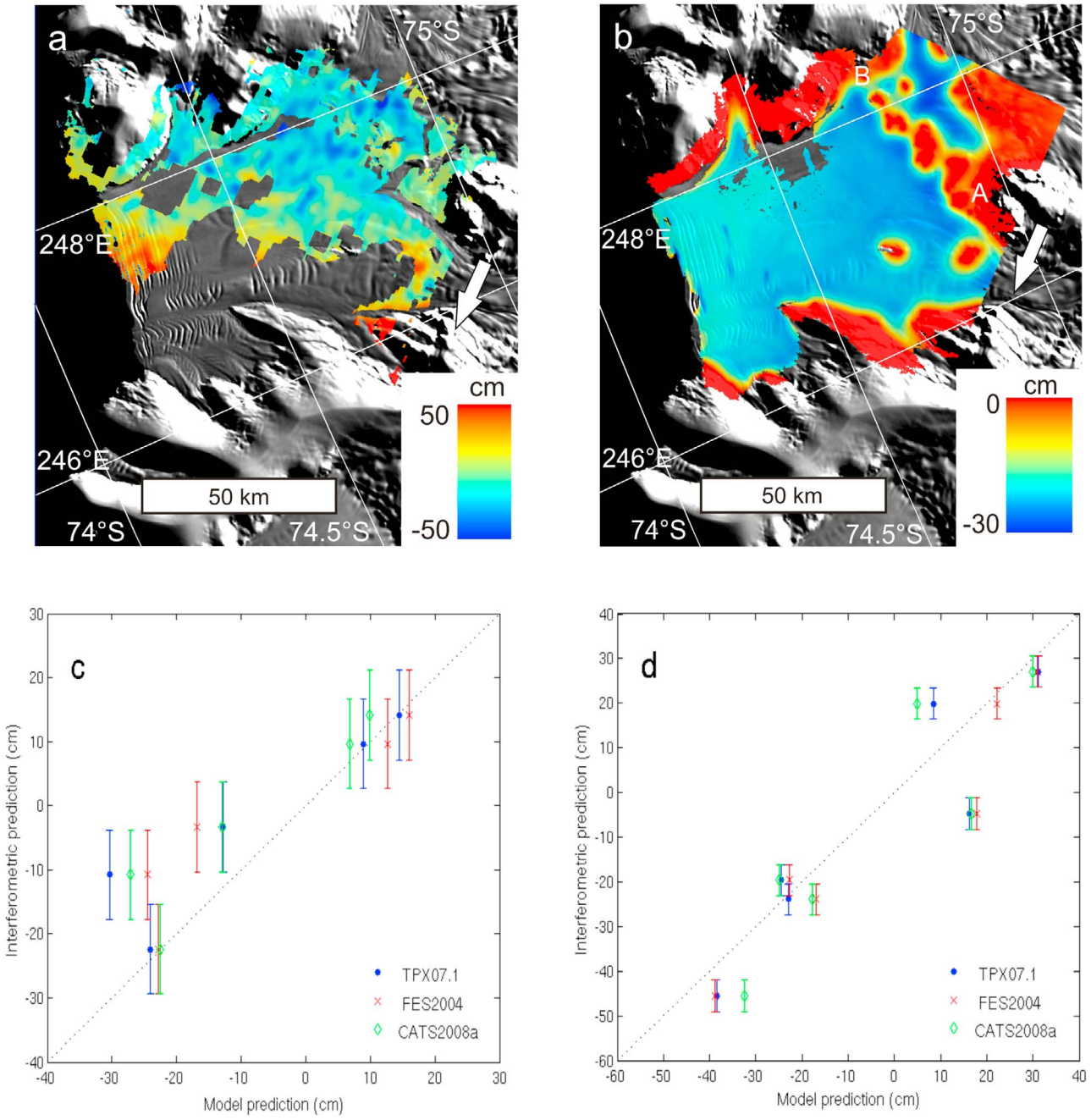

Figure 3. Tidal displacement of the Dotson Ice Shelf. (a) Map of the tidal displacement occurring between 14:57 UTC on 22 February 1994 and 14:57 UTC on 25 February 1994; displacement map determined using single-difference method. (b) Map of the difference in the tidal displacements occurring during the periods 20–23 January 1994 and 23–26 January 1994 (at 14:57 UTC on each day); displacement map determined using double-difference method. (c) Comparison of modeled and observed single-difference tidal motion; observations determined from multiple SAR image pairs (Table 1). (d) Comparison of modeled and observed double-difference tidal motion; observations determined from multiple SAR image pairs (Table 2). In Figures 3a and 3b the white arrow indicates the satellite's ground range (across-track) direction, and the background image is taken from the MODIS mosaic of Antarctica [*Haran et al.*, 2005]. In Figure 3b, A and B bound the locally grounded areas referred to in section 7.2. In Figures 3c and 3d the dashed line indicates equivalence between model predictions and observations, and errors bars represent measurement error as determined in section 6.

region of grounded ice located between A and B in Figure 3b, suggesting that a bedrock ridge underlies the ice at this point. This is coincident with a region of slow flow (Figure 2a). On the freely floating part of the ice shelf, there was little (~1 cm on average) spatial variation in the tidal signal, indicating that the double-difference tide is relatively constant over these length scales, and that there is no residual signal arising from variable flow.

7.3. Tide Model Evaluation

[45] We used our single-difference and double-difference tidal observations to evaluate the FES, TPX, and CATS tide models at the Dotson Ice Shelf. Comparing our single-difference observations to the equivalent tide model predictions (Figure 3c) yielded root-mean-square differences between the observed and modeled tidal displacements of 9.8, 8.8, and 8.7 cm for the TPXO, CATS, and FES models, respectively. The measurement error associated with our single-difference technique is 7 cm (Table 3). At three out of the five epochs, the models agreed extremely well with our observations, with only a ~2 cm root-mean-square difference between the two. We have been unable to determine any distinctive circumstances pertaining to these observations, which could explain the apparent distinction between cases of good and poor agreement.

[46] Comparing our double-difference observations to predictions formed from the three tide models (Figure 3d) gave root-mean-square differences between the observed and modeled tidal signals of 10.5, 12.4, and 10.3 cm for TPXO, CATS, and FES, respectively. The measurement error associated with our double-difference technique is 3.5 cm (Table 3).

8. Discussion

[47] In this study we have used two different InSAR-based methods to assess three tide models. In section 8.1 we assess the relative strengths of the two evaluation methods, in section 8.2 we compare the performance of the three tide models, in section 8.3 we consider the benefits of our inverse barometer approximation for pressure-related ice shelf height changes, and in section 8.4 we place our results within the context of previous studies.

8.1. Comparison of Methods of Observation

[48] We have employed two InSAR-based methods to isolate the tidal motion of an ice shelf; a single-difference method that measures tidal displacement, and a double-difference method that measures changes in tidal displacement. Our assessment of measurement error (section 6) indicates that both techniques are sufficiently accurate to provide useful information regarding the accuracy of the current generation of tide models around Antarctica. However, should polar tide model accuracy approach that of the deep ocean (typically 2–3 cm), the techniques presented here would need to be improved if they were to provide the required accuracy for model evaluation. Comparing our two methods, we found that the double-difference technique provided a clearer picture of the tidal signal, consistent with the smaller error associated with this method, and additionally offered better spatial coverage. This analysis indicates that the double-difference method should be used in work that requires a map of tidal displacement, for example when mapping the grounding line of a glacier [e.g., *Rignot*, 1998].

[49] For certain applications, however, the double-difference method may be unsatisfactory because, in the process of differencing two estimates of tidal displacement, we cancel any systematic error in the model predictions of tidal displacement. An important use of tide models around Antarctica is to simulate the tidal displacement recorded within a single interferogram. This prediction can be used to remove the tidal signal from an interferogram and forms part of a commonly used interferometric method to map ice shelf flow velocity [e.g., *Rignot and Jacobs*, 2002; *Joughin et al.*, 2003; *Rignot et al.*, 2004]. In this case, the error in such predictions of flow, resulting from any unmodeled tidal signal, must be quantified. For this purpose a single-difference technique should be applied, so as to account for both systematic and random errors in model predictions of tidal displacement. Accordingly, we can convert our estimate of single-difference tide model accuracy (e.g., 8.7 cm for FES) into an equivalent horizontal displacement error in the ground range direction. This quantifies the uncertainty introduced into the ground range component of model-dependent velocity estimates, should an unmodeled tidal signal of this magnitude be interpreted as a horizontal flow displacement. In this case, our study suggests that tide model inaccuracies will introduce an error of 22 m/yr into such predictions (range component of velocity only).

[50] Our analysis has shown that our single-difference technique yields relatively imprecise and noisy observations of tidal displacement. A particular problem with these estimates was the ~1 m amplitude long-wavelength variation in tidal displacement across the ice shelf. Neither our double-difference observations nor our model predictions (section 8.2) exhibit a ramp of this magnitude. We therefore conclude that it is an artifact of the processing method used, rather than a real tidal signal. Specifically, we believe it results from errors in our estimation of ice flow (see section 6.3), arising from inaccuracies in the coregistration of the image pair used for intensity tracking. This is due to the coregistration function being poorly constrained over some parts of the ice shelf. To mitigate the effect of the ramp we have limited displacement estimates to regions where the coregistration function is well constrained. Even so, our error analysis suggests that our single-difference measurement error is dominated by errors originating from the coregistration stage of our intensity tracking procedure. This highlights the difficulty of achieving the precision required for tide model evaluations using our single-difference method, particularly at locations lacking stable areas for image coregistration. In other regions, where more extensive stable areas exist, our single-difference technique may provide more precise estimates.

[51] Furthermore, it is possible that additional processing steps could improve image coregistration. For example, the application of a low-pass filter prior to image coregistration could remove short-wavelength surface features and isolate long-wavelength features originating from subice bedrock topography [e.g., *Bindschadler and Scambos*, 1991]. This could allow a more extensive coregistration data set to be derived. We do not apply this technique here because of the

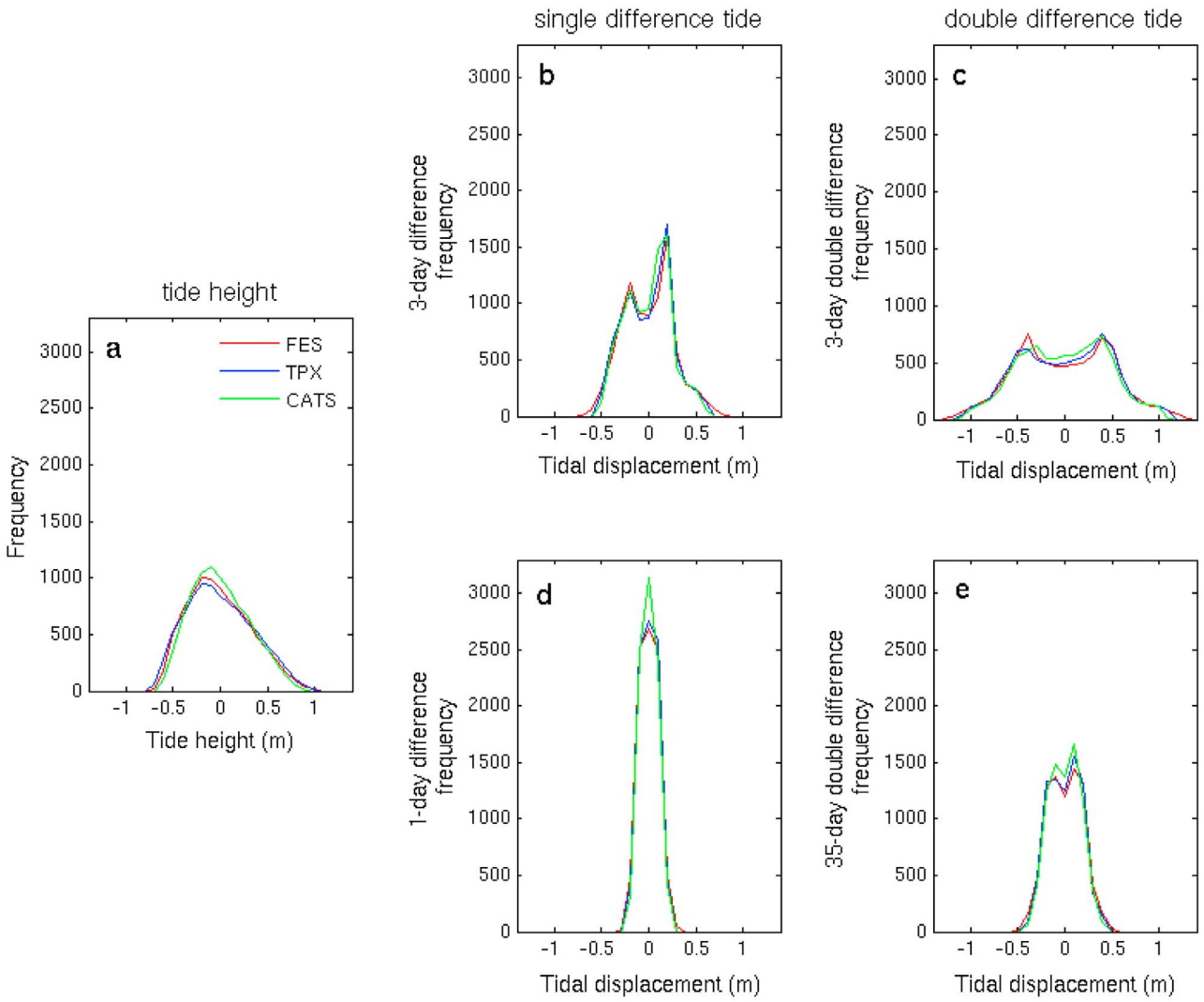

Figure 4. Distribution of hourly modeled tide predictions at the Dotson Ice Shelf, 1994. (a) Tide height, (b) difference in tide height over a 3 day period (i.e., the tidal signal recorded by a 3 day interferogram), (c) double-difference in tide height (i.e., the tidal signal recorded in a differential interferogram, formed from four consecutive SAR images, each separated by 3 days), (d) difference in tide height over a 1 day period (i.e., the tidal signal recorded in a 1 day interferogram), and (e) double difference in tide height (i.e., the tidal signal recorded in a differential interferogram, formed from two 1 day interferograms, with a 35 day separation between the two interferograms).

limited grounded ice present in our images. An alternative approach to minimize the effect of coregistration error would be to measure ice flow (via intensity tracking) over a longer time period. This would reduce the contribution of coregistration error relative to the measured displacement signal. In this study we found that tracking displacement over a longer time period reduced the area over which a coherent displacement signal could be derived, providing insufficient coverage to determine tidal motion. In areas that exhibit more stable surface characteristics, or alternatively by using lower-frequency sensors that penetrate further into the snowpack (such as the L band radar on board the Advanced Land Observation System (ALOS) [*Rignot*, 2008]), it may be possible to reduce the effect of coregistration errors by increasing the time period over which surface features are tracked.

[52] The characteristics of the tidal signals recorded by our single-difference and double-difference methods will vary according to the method used and the time span over which the SAR data were collected (as determined by the satellite repeat time; see Tables 1 and 2). To investigate the impact of these factors upon the amplitude of the tidal signal we simulated the statistics of the single- and double-difference signals from hourly resolution tide model data spanning the year of 1994 (Figure 4). When calculating the single- and double-difference tidal signals, we considered the two scenarios relevant to the orbital characteristics of the data used in this study. For our single-difference technique this was the tidal displacement occurring over a 1 day (ERS-1/2 tandem) and 3 day (ERS-1 ice phase) interval. For our double-difference technique we calculated the signals corresponding to (1) a differential interferogram formed from four SAR

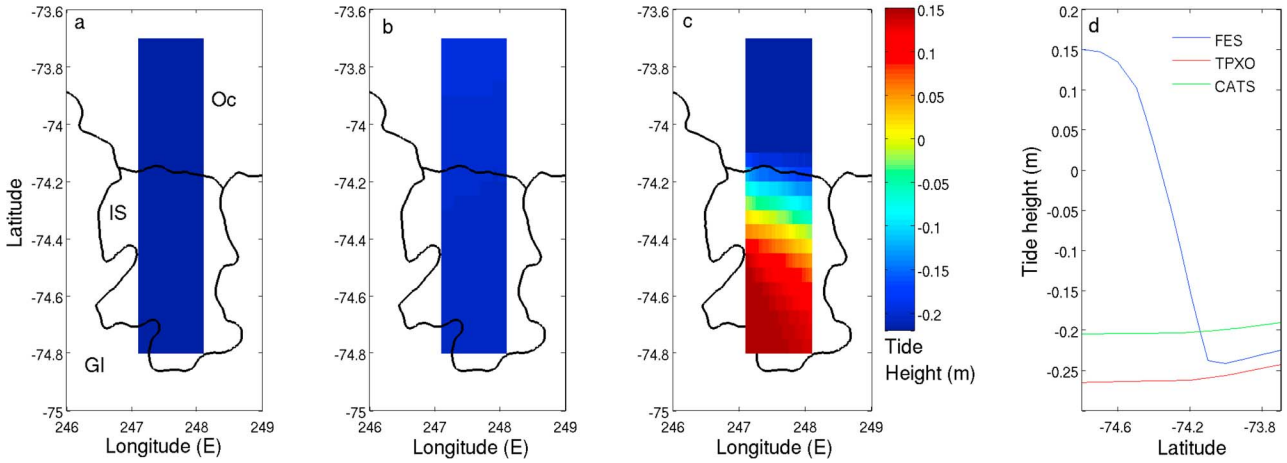

Figure 5. Model predictions of tide height at the Dotson Ice Shelf at 14:50 LT on 3 February 1996. Thick black line in Figures 5a–5c separates the ocean (Oc), the ice shelf (IS), and grounded ice (GI). (a) TPXO, (b) CATS, (c) FES, and (d) north-south transect of modeled tide heights along 247.5°E. The spatial extent of predictions is limited to that of the FES model domain.

images, with each acquisition separated by 3 days (hereafter referred to as 3,3 acquisition mode), and (2) a differential interferogram formed from two interferograms separated by 35 days, with the component SAR images of each interferogram separated by 1 day (hereafter referred to as 1,35 acquisition mode). Figure 4 indicates that the likely magnitude of the tidal signal will vary depending upon which of the two acquisition modes we are in and whether we are measuring single- or double-difference tides. For both single- and double-difference tides we would expect to see a greater sensitivity to the tidal signal in the 3,3 acquisition mode, as compared to the 1,35 acquisition mode. This is to be expected since the 1 day sampling period of the 1,35 acquisition mode results in a greater aliasing of the approximately diurnal and semidiurnal tidal constituents. As a result, the 3,3 acquisition mode provides a more comprehensive evaluation of the modeled tidal signal, although it still does not adequately sample all tidal constituents (e.g., S_2, 12 h period).

[53] For a given acquisition mode, the double-difference technique is likely to resolve a larger tidal signal than the single-difference technique. Consequently, if the aim of a study is to resolve the tidal signal (for example to map the grounding line of a glacier [*Rignot*, 1998]) then it would be preferable to use 3,3 acquisition mode data, along with a double-difference technique. Conversely, if the aim is to minimize the tidal signal, say for estimating ice flow using a single interferogram, then 1,35 acquisition mode data is a better choice.

8.2. Comparison of Tide Models

[54] The three tide models considered here predict the amplitude of the observed single- and double-difference tidal signals with comparable accuracy. In both cases FES marginally outperformed the other two models, but the difference between models was not large. To assess the extent to which model choice affected the simulated tidal amplitude, we investigated the spatial and temporal consistency of the FES, TPXO and CATS tide model predictions in the vicinity of the Dotson Ice Shelf.

[55] Figure 5 illustrates the spatial variability in the tidal amplitude predicted by the three models. Maps of single- and double-difference tidal displacement exhibited similar spatial patterns. Seaward of the ice shelf front, predictions from the three models are relatively consistent. However, upon crossing the ice front, there is a discontinuity in the gradient of the FES solution, and FES tide height rapidly diverges from the other two models. TPXO and CATS retain their consistency over the whole of the ice shelf. Possible sources of the inconsistency of FES may be differing bathymetry used in this region or varying subice shelf water column thickness. Further investigation is required to understand the cause of this discrepancy. The agreement between FES predictions and interferometric observations is far greater seaward of the ice front than on the ice shelf itself, suggesting that the on-shelf ramp in FES tide height (Figures 5c and 5d) is not a real phenomenon. This motivated our decision to use modeled tide heights from just seaward of the ice front, at 74.1°S, 247.5°E (Figure 1). This is not problematic for our work, but in studies where the pattern of tidal displacement over the ice shelf is being modeled, it would be worthwhile checking the consistency of FES with other models, and may provide a reason to favor CATS or TPXO. We note that a similar assessment of FES95.2 at the Filchner-Ronne Ice Shelf [*Rignot et al.*, 2000] found no such discrepancy, and so this issue may only pertain to small ice shelves.

[56] Next we assessed the temporal consistency of model predictions of tide height, and of the tidal signals isolated by our single-difference and double-difference methods. Using results from the three tide models, we formed time series of tide height, 3 day tide height difference, and the double difference in tide height for a monthlong period coincident with part of our SAR data set (Figure 6). All three tide models were generally in good agreement in predicting both the amplitude and the phase of the tidal signal. Intermodel variability was further reduced by differencing and then double differencing the tidal signals (Figures 6d–6f). This analysis is consistent with the results of our InSAR-based model evaluation (section 7.3), which showed little difference in the performance of the three models. Over the monthlong period

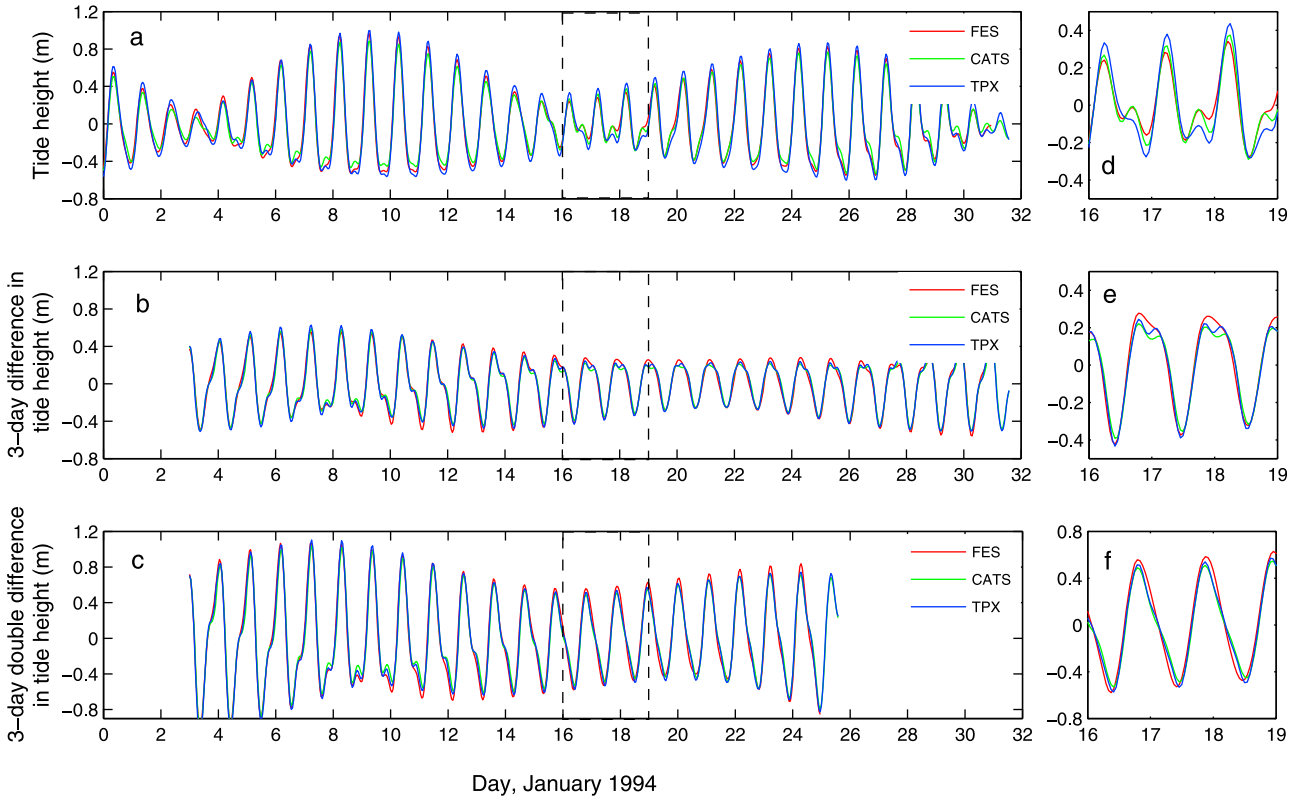

Figure 6. Temporal variability of modeled tide predictions at the Dotson Ice Shelf: January 1994 (Figures 6a–6c) and 3 day period (Figures 6d–6f; period indicated by dashed lines in Figures 6a–6c) showing differences between models. (a, d) Tide height, (b, e) difference in tide height over a 3 day period (i.e., the tidal signal recorded in a 3 day interferogram), (c, f) double difference in tide height (i.e., the tidal signal recorded in a differential interferogram, formed from two consecutive 3 day interferograms).

considered here, the longer-period (greater than diurnal) variability was reduced in the differenced and double-differenced tidal signal. This analysis (Figure 6) also indicates that semidiurnal tides are relatively weak at the Dotson Ice Shelf.

8.3. Assessment of Inverse Barometer Correction

[57] In situations where in situ meteorological records are located close to the study site, an inverse barometer correction based upon such measurements can substantially improve InSAR-based assessments of tide models [*Padman et al.*, 2003b]. What has been less clear is whether, in the absence of such records, model data are sufficiently accurate to merit being used as the basis for inverse barometer corrections. Additionally, previous studies [e.g., *Ponte et al.*, 1991] have indicated that an inverse barometer model may not be appropriate over the 1 day time scales at which some of our data (Table 2) were collected. To investigate these issues, we compared our single- and double-difference results, both with and without inverse barometer corrections. We found that, for all models considered here, and for both the single- and double-difference results, the inclusion of the correction improved the agreement between observations and model predictions by an average of 6%. This suggests that the accuracy of model reanalysis pressure fields and the validity of the inverse barometer approximation are sufficient to model, at least in part, ice shelf displacement arising from atmospheric pressure changes over these time scales. It is possible that a more sophisticated model-based correction for atmospheric pressure loading [e.g., *Carrere and Lyard*, 2003] may provide further improvement over short time scales.

8.4. Comparison to Previous Work

[58] To our knowledge, only one study [*Rignot*, 2002] has provided an evaluation of tide model predictions in the Amundsen Sea. Our results find a similar degree of agreement between double-difference observations and model predictions to that of *Rignot* [2002]. Studying the nearby Pine Island Ice Shelf, *Rignot* [2002] found the accuracy of FES99 (a predecessor of FES2004) double-difference predictions to be 9 cm. Here we find the equivalent (no inverse barometer correction) root-mean-square difference to be 10.6 cm. Other tide model evaluations have been conducted around Antarctica on the basis of both remote sensing [*Padman et al.*, 2003a] and in situ [*King and Padman*, 2005; *King et al.*, 2011] data. Variations in these error estimates arise because of differences in (1) the models evaluated, (2) the evaluation methods used, (3) the error metric chosen, and (4) the tidal characteristics of the region in which the analysis was performed. Nonetheless, the studies conducted by *Rignot* [2002], *Padman et al.* [2003a], *King and Padman* [2005], and *King et al.* [2011], together with the work described here, paint a

broadly consistent picture of approximately decimeter-level tide model accuracy in Antarctic coastal waters.

9. Conclusions

[59] In this study we have developed InSAR-based estimates of ice shelf tidal motion in order to assess the accuracy with which ocean tide models can predict ice shelf tidal motion in remote regions of Antarctica. Firstly, we used a single-difference technique to assess the ability of tide models to predict changes in tide height. Secondly, we used a double-difference technique to evaluate model predictions of the difference between two tidal displacements. Comparing these two methods, we find that the double-difference technique, with a 3.5 cm measurement error, provides a more accurate assessment of tidal displacement. Three tide models (TPXO7.1, CATS2008a_opt, and FES2004) perform comparably well, with root-mean-square deviations from observations of ~9 cm (single-difference technique) and ~10 cm (double-difference technique). We find here that FES predictions coincident with the ice shelf itself are not reliable. The inclusion of a model-based correction for atmospheric pressure fluctuations improves the agreement between tide model predictions and observations, suggesting that the accuracy of model reanalysis pressure fields is sufficient to merit the application of such a model-based correction.

[60] The single-difference approach, unlike its double-difference counterpart, directly assesses the accuracy with which tide models can reproduce the tidal signal recorded in an interferogram. This quantifies the tidal error in model-dependent InSAR estimates of ice flow, which results from model inaccuracies in predicting tidal displacement. Our study indicates that the tide models considered here can reproduce daily-scale tidally induced ice shelf height changes in the Amundsen Sea to an accuracy of ~9 cm. This would equate to an error of 22 m/yr in the ground range component of the velocity field if this unmodeled tidal signal was interpreted as ice shelf flow. This level of accuracy is comparable to other regions around Antarctica, where there is a higher prevalence of in situ tidal records. The methods described here can be used to evaluate tide models in other remote Antarctic waters.

[61] **Acknowledgments.** This work was funded by the UK Natural Environment Research Council's National Centre for Earth Observation, through a Centre for Polar Observation and Modeling Ph.D. studentship. We acknowledge the British Atmospheric Data Centre for supplying the ECMWF data and the ESA VECTRA program for the provision of the raw SAR data. We are grateful to the architects of the FES, TPXO, and CATS tide models for making their models freely available. We thank Noel Gourmelen for reviewing a draft version of the manuscript and Laurie Padman and one anonymous reviewer for their thoughtful reviews, which helped to substantially improve the manuscript.

References

Bamber, J. L., and R. A. Bindschadler (1997), An improved elevation dataset for climate and ice-sheet modelling: Validation with satellite imagery, *Ann. Glaciol.*, *25*, 438–444.

Bamber, J., and J. L. Gomez-Dans (2005), The accuracy of digital elevation models of the Antarctic continent, *Earth Planet. Sci. Lett.*, *237*(3–4), 516–523, doi:10.1016/j.epsl.2005.06.008.

Bamber, J. L., J. L. Gomez-Dans, and J. A. Griggs (2009), A new 1 km digital elevation model of the Antarctic derived from combined satellite radar and laser data—Part 1: Data and methods, *Cryosphere*, *3*(1), 101–111.

Bindschadler, R., and T. Scambos (1991), Satellite-image-derived velocity field of an Antarctic ice stream, *Science*, *252*(5003), 242–246.

Carrere, L., and F. Lyard (2003), Modeling the barotropic response of the global ocean to atmospheric wind and pressure forcing—Comparisons with observations, *Geophys. Res. Lett.*, *30*(6), 1275, doi:10.1029/2002GL016473.

Cook, A. J., and D. G. Vaughan (2010), Overview of areal changes of the ice shelves on the Antarctic Peninsula over the past 50 years, *Cryosphere*, *4*(1), 77–98.

De Angelis, H., and P. Skvarca (2003), Glacier surge after ice shelf collapse, *Science*, *299*(5612), 1560–1562.

Egbert, G., and S. Erofeeva (2002), Efficient inverse modeling of barotropic ocean tides, *J. Atmos. Oceanic Technol.*, *19*(2), 183–204.

Egbert, G., A. Bennett, and M. Foreman (1994), TOPEX/Poseidon tides estimated using a global inverse model, *J. Geophys. Res.*, *99*(C12), 24,821–24,852.

Emardson, T. R., M. Simons, and F. H. Webb (2003), Neutral atmospheric delay in interferometric synthetic aperture radar applications: Statistical description and mitigation, *J. Geophys. Res.*, *108*(B5), 2231, doi:10.1029/2002JB001781.

Fricker, H. A., and L. Padman (2002), Tides on Filchner-Ronne Ice Shelf from ERS radar altimetry, *Geophys. Res. Lett.*, *29*(12), 1622, doi:10.1029/2001GL014175.

Goldstein, R. (1995), Atmospheric limitations to repeat-track radar interferometry, *Geophys. Res. Lett.*, *22*(18), 2517–2520.

Goldstein, R., H. Zebker, and C. Werner (1988), Satellite radar interferometry: Two-dimensional phase unwrapping, *Radio Sci.*, *23*(4), 713–720.

Goldstein, R., H. Engelhardt, B. Kamb, and R. Frolich (1993), Satellite radar interferometry for monitoring ice-sheet motion: Application to an Antarctic ice stream, *Science*, *262*(5139), 1525–1530.

Gray, A. L., K. E. Mattar, and G. Sofko (2000), Influence of ionospheric electron density fluctuations on satellite radar interferometry, *Geophys. Res. Lett.*, *27*(10), 1451–1454.

Hanssen, R. (2001), *Radar Interferometry: Data Interpretation and Error Analysis*, Kluwer Acad., Dordrecht, Netherlands.

Haran, T., J. Bohlander, T. Scambos, T. Painter, and M. Fahnestock (2005), MODIS mosaic of Antarctica (MOA) image map, Natl. Snow and Ice Data Cent., Boulder, Colo. [Updated 2006.]

Hartl, P., K. Thiel, X. Wu, C. Doake, and J. Sievers (1994), Application of SAR interferometry with ERS-1 in the Antarctic, *Earth Obs. Q.*, *43*, 1–4.

Jenkins, A., P. Dutrieux, S. S. Jacobs, S. D. McPhail, J. R. Perrett, A. T. Webb, and D. White (2010), Observations beneath Pine Island Glacier in West Antarctica and implications for its retreat, *Nat. Geosci.*, *3*(7), 468–472, doi:10.1038/ngeo890.

Joughin, I., and L. Padman (2003), Melting and freezing beneath Filchner-Ronne Ice Shelf, Antarctica, *Geophys. Res. Lett.*, *30*(9), 1477, doi:10.1029/2003GL016941.

Joughin, I., D. Winebrenner, and M. Fahnestock (1995), Observations of ice-sheet motion in Greenland using satellite radar interferometry, *Geophys. Res. Lett.*, *22*(5), 571–574.

Joughin, I., R. Kwok, and M. Fahnestock (1996a), Estimation of ice-sheet motion using satellite radar interferometry: Method and error analysis with application to Humboldt Glacier, Greenland, *J. Glaciol.*, *42*(142), 564–575.

Joughin, I., D. Winebrenner, M. Fahnestock, R. Kwok, and W. Krabill (1996b), Measurement of ice-sheet topography using satellite radar interferometry, *J. Glaciol.*, *42*(140), 10–22.

Joughin, I., R. Kwok, and M. Fahnestock (1998), Interferometric estimation of three-dimensional ice-flow using ascending and descending passes, *IEEE Trans. Geosci. Remote Sens.*, *36*(1), 25–37.

Joughin, I., E. Rignot, C. E. Rosanova, B. K. Lucchitta, and J. Bohlander (2003), Timing of recent accelerations of Pine Island Glacier, Antarctica, *Geophys. Res. Lett.*, *30*(13), 1706, doi:10.1029/2003GL017609.

King, J. C. (2003), Validation of ECMWF sea level pressure analyses over the Bellingshausen Sea, Antarctica, *Weather Forecast.*, *18*(3), 536–540.

King, M., and L. Padman (2005), Accuracy assessment of ocean tide models around Antarctica, *Geophys. Res. Lett.*, *32*, L23608, doi:10.1029/2005GL023901.

King, M., L. Padman, K. Nicholls, P. Clarke, G. H. Gudmundsson, B. Kulessa, and A. Shepherd (2011), Ocean tides in the Weddell Sea: New observations on the Filchner-Ronne and Larsen C ice shelves and model validation, *J. Geophys. Res.*, *116*, C06006, doi:10.1029/2011JC006949.

Kwok, R., and M. A. Fahnestock (1996), Ice sheet motion and topography from radar interferometry, *IEEE Trans. Geosci. Remote Sens.*, *34*(1), 189–200.

Luckman, A., T. Murray, H. Jiskoot, H. Pritchard, and T. Strozzi (2003), ERS SAR feature-tracking measurement of outlet glacier velocities on a regional scale in east Greenland, *Ann. Glaciol.*, *36*, 129–134.

Lyard, F., F. Lefevre, T. Letellier, and O. Francis (2006), Modelling the global ocean tides: Modern insights from FES2004, *Ocean Dyn.*, *56*(5–6), 394–415, doi:10.1007/s10236-006-0086-x.

Makinson, K., P. Holland, A. Jenkins, K. Nicholls, and D. Holland (2011), Influence of tides on melting and freezing beneath Filchner-Ronne Ice Shelf, Antarctica, *Geophys. Res. Lett.*, *38*, L06601, doi:10.1029/2010GL046462.

Massom, R., and D. Lupin (2006), *Polar Remote Sensing*, vol. 2, *Ice Sheets*, Praxis, Chichester, U. K.

Massonnet, D., and K. L. Feigl (1998), Radar interferometry and its application to changes in the Earth's surface, *Rev. Geophys.*, *36*(4), 441–500.

Mattar, K. E., and A. L. Gray (2002), Reducing ionospheric electron density errors in satellite radar interferometry applications, *Can. J. Remote Sens.*, *28*(4), 593–600.

McMillan, M., A. Shepherd, D. G. Vaughan, S. Laxon, and D. McAdoo (2009), Amundsen Sea bathymetry: The benefits of using gravity data for bathymetric prediction, *IEEE Trans. Geosci. Remote Sens.*, *47*(12), 4223–4228, doi:10.1109/TGRS.2009.2023665.

Nitsche, F., S. Jacobs, R. Larter, and K. Gohl (2007), Bathymetry of the Amundsen Sea continental shelf: Implications for geology, oceanography, and glaciology, *Geochem. Geophys. Geosyst.*, *8*, Q10009, doi:10.1029/2007GC001694.

Padman, L., and H. A. Fricker (2005), Tides on the Ross Ice Shelf observed with ICESat, *Geophys. Res. Lett.*, *32*, L14503, doi:10.1029/2005GL023214.

Padman, L., H. Fricker, R. Coleman, S. Howard, and L. Erofeeva (2002), A new tide model for the Antarctic ice shelves and seas, *Ann. Glaciol.*, *34*(1), 247–254, doi:10.3189/172756402781817752.

Padman, L., S. Erofeeva, and I. Joughin (2003a), Tides of the Ross Sea and Ross Ice Shelf cavity, *Antarct. Sci.*, *15*, 31–40, doi:10.1017/S0954102003001032.

Padman, L., M. King, D. Goring, H. Corr, and R. Coleman (2003b), Ice-shelf elevation changes due to atmospheric pressure variations, *J. Glaciol.*, *49*(167), 521–526.

Payne, A., A. Vieli, A. Shepherd, D. Wingham, and E. Rignot (2004), Recent dramatic thinning of largest West Antarctic ice stream triggered by oceans, *Geophys. Res. Lett.*, *31*, L23401, doi:10.1029/2004GL021284.

Payne, A., P. Holland, A. Shepherd, I. Rutt, A. Jenkins, and I. Joughin (2007), Numerical modeling of ocean-ice interactions under Pine Island Bay's ice shelf, *J. Geophys. Res.*, *112*, C10019, doi:10.1029/2006JC003733.

Pfeffer, W. T., J. T. Harper, and S. O'Neel (2008), Kinematic constraints on glacier contributions to 21st-century sea-level rise, *Science*, *321*(5894), 1340–1343, doi:10.1126/science.1159099.

Ponte, R., D. Salstein, and R. Rosen (1991), Sea-level response to pressure forcing in a barotropic numerical model, *J. Phys. Oceanogr.*, *21*(7), 1043–1057, doi:10.1175/1520-0485.

Pritchard, H., T. Murray, A. Luckman, T. Strozzi, and S. Barr (2005), Glacier surge dynamics of Sortebrae, east Greenland, from synthetic aperture radar feature tracking, *J. Geophys. Res.*, *110*, F03005, doi:10.1029/2004JF000233.

Pritchard, H. D., R. J. Arthern, D. G. Vaughan, and L. A. Edwards (2009), Extensive dynamic thinning on the margins of the Greenland and Antarctic ice sheets, *Nature*, *461*(7266), 971–975, doi:10.1038/nature08471.

Ray, R., D. Rowlands, and G. Egbert (2003), Tidal models in a new era of satellite gravimetry, *Space Sci. Rev.*, *108*(1–2), 271–282.

Rignot, E. (1996), Tidal motion, ice velocity and melt rate of Petermann Gletscher, Greenland, measured from radar interferometry, *J. Glaciol.*, *42*(142), 476–485.

Rignot, E. (1998), Fast recession of a West Antarctic glacier, *Science*, *281*(5376), 549–551.

Rignot, E. (2002), Ice-shelf changes in Pine Island Bay, Antarctica, 1947–2000, *J. Glaciol.*, *48*(161), 247–256.

Rignot, E. (2006), Changes in ice dynamics and mass balance of the Antarctic ice sheet, *Philos. Trans. R. Soc. A*, *364*(1844), 1637–1655, doi:10.1098/rsta.2006.1793.

Rignot, E. (2008), Changes in West Antarctic ice stream dynamics observed with ALOS PALSAR data, *Geophys. Res. Lett.*, *35*, L12505, doi:10.1029/2008GL033365.

Rignot, E., and S. S. Jacobs (2002), Rapid bottom melting widespread near Antarctic ice sheet grounding lines, *Science*, *296*(5575), 2020–2023.

Rignot, E., and D. MacAyeal (1998), Ice-shelf dynamics near the front of the Filchner-Ronne Ice Shelf, Antarctica, revealed by SAR interferometry, *J. Glaciol.*, *44*(147), 405–418.

Rignot, E., L. Padman, D. MacAyeal, and M. Schmeltz (2000), Observation of ocean tides below the Filchner and Ronne Ice Shelves, Antarctica, using synthetic aperture radar interferometry: Comparison with tide model predictions, *J. Geophys. Res.*, *105*(C8), 19,615–19,630.

Rignot, E., G. Casassa, P. Gogineni, W. Krabill, A. Rivera, and R. Thomas (2004), Accelerated ice discharge from the Antarctic Peninsula following the collapse of Larsen B ice shelf, *Geophys. Res. Lett.*, *31*, L18401, doi:10.1029/2004GL020697.

Rignot, E., et al. (2005), Recent ice loss from the Fleming and other glaciers, Wordie Bay, West Antarctic Peninsula, *Geophys. Res. Lett.*, *32*, L07502, doi:10.1029/2004GL021947.

Rignot, E., J. Bamber, M. Van Den Broeke, C. Davis, Y. Li, W. Van De Berg, and E. Van Meijgaard (2008), Recent Antarctic ice mass loss from radar interferometry and regional climate modelling, *Nat. Geosci.*, *1*(2), 106–110, doi:10.1038/ngeo102.

Rodriguez, E., and J. Martin (1992), Theory and design of interferometric synthetic aperture radars, *IEE Proc. F, Radar Signal Process.*, *139*(2), 147–159.

Rott, H., P. Skvarca, and T. Nagler (1996), Rapid collapse of northern Larsen Ice Shelf, Antarctica, *Science*, *271*(5250), 788–792.

Scambos, T., H. Fricker, C. Liu, J. Bohlander, J. Fastook, A. Sargent, R. Massom, and A. Wu (2009), Ice shelf disintegration by plate bending and hydro-fracture: Satellite observations and model results of the 2008 Wilkins ice shelf break-ups, *Earth Planet. Sci. Lett.*, *280*(1–4), 51–60, doi:10.1016/j.epsl.2008.12.027.

Shepherd, A., and N. Peacock (2003), Ice shelf tidal motion derived from ERS altimetry, *J. Geophys. Res.*, *108*(C6), 3198, doi:10.1029/2001JC001152.

Shepherd, A., D. Wingham, and J. Mansley (2002), Inland thinning of the Amundsen Sea sector, West Antarctica, *Geophys. Res. Lett.*, *29*(10), 1364, doi:10.1029/2001GL014183.

Shepherd, A., D. Wingham, and E. Rignot (2004), Warm ocean is eroding West Antarctic Ice Sheet, *Geophys. Res. Lett.*, *31*, L23402, doi:10.1029/2004GL021106.

Shepherd, A., D. Wingham, D. Wallis, K. Giles, S. Laxon, and A. V. Sundal (2010), Recent loss of floating ice and the consequent sea level contribution, *Geophys. Res. Lett.*, *37*, L13503, doi:10.1029/2010GL042496.

Strozzi, T., A. Luckman, T. Murray, U. Wegmuller, and C. Werner (2002), Glacier motion estimation using SAR offset-tracking procedures, *IEEE Trans. Geosci. Remote Sens.*, *40*(11), 2384–2391, doi:10.1109/tgrs.2002.805079.

Sugden, D. (2009), *Ice Sheets and Ice Caps*, chap. 14, pp. 368–402, Cambridge Univ. Press, Cambridge, U. K.

Thoma, M., A. Jenkins, D. Holland, and S. Jacobs (2008), Modelling Circumpolar Deep Water intrusions on the Amundsen Sea continental shelf, Antarctica, *Geophys. Res. Lett.*, *35*, L18602, doi:10.1029/2008GL034939.

Trenberth, K., J. Fasullo, and L. Smith (2005), Trends and variability in column-integrated atmospheric water vapor, *Clim. Dyn.*, *24*(7–8), 741–758, doi:10.1007/s00382-005-0017-4.

Uppala, S., et al. (2005), The ERA-40 re-analysis, *Q. J. R. Meteorol. Soc.*, *131*(612), 2961–3012, doi:10.1256/qj.04.176.

Vaughan, D. G., and C. S. M. Doake (1996), Recent atmospheric warming and retreat of ice shelves on the Antarctic Peninsula, *Nature*, *379*(6563), 328–331.

Vieli, A., A. Payne, Z. Du, and A. Shepherd (2006), Numerical modelling and data assimilation of the Larsen B ice shelf, Antarctic Peninsula, *Philos. Trans. R. Soc. A*, *364*(1844), 1815–1839, doi:10.1098/rsta.2006.1800.

Vieli, A., A. Payne, A. Shepherd, and Z. Du (2007), Causes of pre-collapse changes of the Larsen B ice shelf: Numerical modelling and assimilation of satellite observations, *Earth Planet. Sci. Lett.*, *259*(3–4), 297–306, doi:10.1016/j.epsl.2007.04.050.

Werner, C., U. Wegmuller, T. Strozzi, and A. Wiesmann (2000), Gamma SAR and interferometric processing software, paper presented at ERS-Envisat Symposium, Eur. Space Agency, Gothenburg, Sweden.

Werner, C., T. Strozzi, A. Wiesmann, U. Wegmuller, T. Murray, L. Pritchard, and A. Luckman (2001), Complimentary measurement of geophysical deformation using repeat-pass SAR, in *Proceedings of the Geoscience and Remote Sensing Symposium, IGARSS '01*, pp. 3255–3258, IEEE Press, Piscataway, N. J.

Wingham, D., D. Wallis, and A. Shepherd (2009), Spatial and temporal evolution of Pine Island Glacier thinning, 1995–2006, *Geophys. Res. Lett.*, *36*, L17501, doi:10.1029/2009GL039126.

Zebker, H., and Villasenor (1992), Decorrelation in interferometric radar echoes, *IEEE Trans. Geosci. Remote Sens.*, *30*(5), 950–959.

A. Leeson, M. McMillan, and A. Shepherd, School of Earth and Environment, University of Leeds, Leeds LS2 9JT, UK. (m.mcmillan@leeds.ac.uk)

P. Nienow, School of Geosciences, University of Edinburgh, Drummond Street, Edinburgh EH8 9XP, UK.